

PAPER

Unified neutron star EOSs and neutron star structures in RMF models

To cite this article: Cheng-Jun Xia *et al* 2022 *Commun. Theor. Phys.* **74** 095303

View the [article online](#) for updates and enhancements.

You may also like

- [Nuclear symmetry energy and neutron skin thickness of \$^{208}\text{Pb}\$ using a finite range effective interaction](#)
D Behera, S K Tripathy, T R Routray et al.
- [Nuclear symmetry energy parameters from neutron skin thickness in \$^{208}\text{Pb}\$ and electric dipole polarizability in \$^{68}\text{Ni}\$, \$^{120}\text{Sn}\$ and \$^{208}\text{Pb}\$](#)
Dipanjali Behera, S K Tripathy, T R Routray et al.
- [Influence of direct Urca on the \$r\$ -mode spin down features of newborn neutron star pulsars](#)
T R Routray, S P Pattnaik, C Gonzalez-Boquera et al.

Unified neutron star EOSs and neutron star structures in RMF models

Cheng-Jun Xia^{1,2,3,*}, Toshiki Maruyama³, Ang Li⁴, Bao Yuan Sun^{5,6},
Wen-Hui Long^{5,6} and Ying-Xun Zhang^{7,8}

¹ Center for Gravitation and Cosmology, College of Physical Science and Technology, Yangzhou University, Yangzhou 225009, China

² School of Information Science and Engineering, NingboTech University, Ningbo 315100, China

³ Advanced Science Research Center, Japan Atomic Energy Agency, Shirakata 2-4, Tokai, Ibaraki 319-1195, Japan

⁴ Department of Astronomy, Xiamen University, Xiamen 361005, China

⁵ School of Nuclear Science and Technology, Lanzhou University, Lanzhou 730000, China

⁶ Frontiers Science Center for Rare Isotopes, Lanzhou University, Lanzhou 730000, China

⁷ China Institute of Atomic Energy, Beijing 102413, China

⁸ Guangxi Key Laboratory Breeding Base of Nuclear Physics and Technology, Guilin 541004, China

E-mail: cjxia@yzu.edu.cn, maruyama.toshiki@jaea.go.jp, liang@xmu.edu.cn, sunby@lzu.edu.cn, longwh@lzu.edu.cn and zhyx@ciae.ac.cn

Received 23 March 2022, revised 24 April 2022

Accepted for publication 23 May 2022

Published 15 August 2022



CrossMark

Abstract

In the framework of the Thomas-Fermi approximation, we systematically study the EOSs and microscopic structures of neutron star matter in a vast density range with $n_b \approx 10^{-10}$ – 2 fm^{-3} , where various covariant density functionals are adopted, i.e., those with nonlinear self couplings (NL3, PK1, TM1, GM1, MTVTC) and density-dependent couplings (DD-LZ1, DDME-X, PKDD, DDME2, DD2, TW99). It is found that the EOSs generally coincide with each other at $n_b \lesssim 10^{-4} \text{ fm}^{-3}$ and $0.1 \text{ fm}^{-3} \lesssim n_b \lesssim 0.3 \text{ fm}^{-3}$, while in other density regions they are sensitive to the effective interactions between nucleons. By adopting functionals with a larger slope of symmetry energy L , the curvature parameter K_{sym} and neutron drip density generally increases, while the droplet size, proton number of nucleus, core-crust transition density, and onset density of non-spherical nuclei, decrease. All functionals predict neutron stars with maximum masses exceeding the two-solar-mass limit, while those of DD2, DD-LZ1, DD-ME2, and DDME-X predict optimum neutron star radii according to the observational constraints. Nevertheless, the corresponding skewness coefficients J are much larger than expected, while only the functionals MTVTC and TW99 meet the start-of-art constraints on J . More accurate measurements on the radius of PSR J0740 + 6620 and the maximum mass of neutron stars are thus essential to identify the functional that satisfies all constraints from nuclear physics and astrophysical observations. Approximate linear correlations between neutron stars' radii at $M = 1.4M_\odot$ and $2M_\odot$, the slope L and curvature parameter K_{sym} of symmetry energy are observed as well, which are mainly attributed to the curvature-slope correlations in the functionals adopted here. The results presented here are applicable for investigations of the structures and evolutions of compact stars in a unified manner.

Supplementary material for this article is available [online](#)

Keywords: neutron star EOS, nuclear pasta, covariant density functionals

(Some figures may appear in colour only in the online journal)

* Author to whom any correspondence should be addressed.

1. Introduction

Due to the challenges residing in simulating dense matter with lattice QCD, the state and composition of stellar matter inside compact stars is still unclear and exhibits large ambiguities. In particular, the uncertainties in the equation of state (EOS) and the corresponding microscopic structures are still sizable [1–5], which were shown to play important roles in the properties and evolutions of compact stars [6–19]. The properties of nuclear matter around the saturation density ($n_0 \approx 0.16 \text{ fm}^{-3}$), on the contrary, are well constrained by various terrestrial experiments, astrophysical observations, and nuclear theories, where the binding energy is $B \approx -16 \text{ MeV}$, the incompressibility $K = 240 \pm 20 \text{ MeV}$ [20], the symmetry energy $S = 31.7 \pm 3.2 \text{ MeV}$ and its slope $L = 58.7 \pm 28.1 \text{ MeV}$ [21, 22]. Note that those quantities can be further constrained by considering the up-to-date astrophysical observations, heavy ion collision data, measurements of the neutron skin thickness for ^{208}Pb in PREX-II [23], as well as predictions of chiral effective field theory, e.g., those in [24, 25]. Meanwhile, at vanishing densities, the interaction among nucleons is negligible so that nuclear matter exhibits a gas phase with well-understood properties [26, 27].

At subsaturation densities, due to the liquid-gas phase transition of nuclear matter, a mixed phase with various nonuniform structures is expected, i.e., nuclear pasta [28–32], which is typically found in the crusts of neutron stars and the core region of supernovae at the stage of gravitational collapse. By employing spherical and cylindrical approximations for the Wigner-Seitz (WS) cell [33–37], five types of geometrical structures for nuclear pasta were obtained aside from the uniform phase, i.e. droplets, rods, slabs, tubes, and bubbles, while further investigations have revealed more complicated structures [38–50]. Nevertheless, the investigation of the EOSs and microscopic structures of nuclear pasta is still far from complete due to the uncertainties in the nuclear energy density functional [51–57], while a unified treatment is preferred so that the uncertainties do not get larger [53, 56].

For stellar matter at larger densities, as we are entering the multimessenger era, constraining the EOS with pulsar observations has reached unprecedented accuracy. For example, the observation of two-solar-mass pulsars [58–62] has excluded various soft EOSs for dense stellar matter. The multi-messenger observations of the binary neutron star merger event GRB 170817A-GW170817-AT 2017gfo have constrained the tidal deformability of $1.4M_\odot$ neutron star with $70 \leq \Lambda_{1.4} \leq 580$ and the radii $R = 11.9 \pm 1.4 \text{ km}$ [63], indicating a soft EOS at small densities. Additionally, based on pulse-profile modeling with NICER and XMM-Newton data, the simultaneous measurements of the masses and radii for PSR J0030 + 0451 and PSR J0740 + 6620 [64–67] suggest that their radii are similar ($\sim 12.4 \text{ km}$) despite the large differences in masses. In such cases, the likelihood of a strong first-order phase transition inside two-solar-mass pulsars may be reduced [68].

The purpose of our current study is twofold. First, we examine the structures of neutron stars without introducing any new degrees of freedom that lead to first-order phase transitions. Since the radius and crust thickness of a neutron star are sensitive to the EOSs [53], a unified description for

neutron star matter is thus necessary [53, 56]. This leads to the second purpose of our study, where we have obtained 11 EOSs and the corresponding microscopic structures of neutron star matter in a unified manner adopting the numerical recipe proposed in [69]. In particular, as was done in [35, 70–72], the properties of nuclear matter are fixed with relativistic mean field (RMF) models [73], which were very successful in describing finite nuclei [73–82] and nuclear matter [83–90]. Two types of RMF Lagrangian are considered, i.e., those with nonlinear self couplings (NL3 [91], PK1 [92], TM1 [93], GM1 [94], MTVTC [35]) and density-dependent couplings (DD-LZ1 [95], DDME-X [96], PKDD [92], DD-ME2 [97], DD2 [98], TW99 [80]).

The paper is organized as follows. In section 2 we present the theoretical framework for the covariant density functionals adopted here and fix the microscopic structures of neutron star matter. The obtained EOSs and microscopic structures of neutron star matter are presented in section 3, while the corresponding neutron star structures and the possible correlations with the symmetry energy coefficients are investigated. We draw our conclusion in section 4

2. Theoretical framework

2.1. RMF models

The Lagrangian density of RMF models for the neutron star matter considered here reads

$$\begin{aligned} \mathcal{L} = & \sum_{i=n,p} \bar{\psi}_i [i\gamma^\mu \partial_\mu - \gamma^0 (g_\omega \omega + g_\rho \rho \tau_i + A q_i) - m_i^*] \psi_i \\ & + \sum_{l=e,\mu} \bar{\psi}_l [i\gamma^\mu \partial_\mu - m_l + e\gamma^0 A] \psi_l - \frac{1}{4} A_{\mu\nu} A^{\mu\nu} \\ & + \frac{1}{2} \partial_\mu \sigma \partial^\mu \sigma - \frac{1}{2} m_\sigma^2 \sigma^2 - \frac{1}{4} \omega_{\mu\nu} \omega^{\mu\nu} + \frac{1}{2} m_\omega^2 \omega^2 \\ & - \frac{1}{4} \rho_{\mu\nu} \rho^{\mu\nu} + \frac{1}{2} m_\rho^2 \rho^2 + U(\sigma, \omega), \end{aligned} \quad (1)$$

where $\tau_n = -\tau_p = 1$ is the 3rd component of isospin, $q_i = e(1 - \tau_i)/2$ the charge, and $m_{n,p}^* \equiv m_{n,p} + g_\sigma \sigma$ the effective nucleon mass. The boson fields σ , ω , ρ , and A take mean values with only the time components due to time-reversal symmetry. Then the field tensors $\omega_{\mu\nu}$, $\rho_{\mu\nu}$, and $A_{\mu\nu}$ vanish except for

$$\omega_{i0} = -\omega_{0i} = \partial_i \omega, \quad \rho_{i0} = -\rho_{0i} = \partial_i \rho, \quad A_{i0} = -A_{0i} = \partial_i A.$$

The nonlinear self couplings of the mesons are determined by

$$U(\sigma, \omega) = -\frac{1}{3} g_2 \sigma^3 - \frac{1}{4} g_3 \sigma^4 + \frac{1}{4} c_3 \omega^4, \quad (2)$$

which effectively account for the in-medium effects and are essential for the covariant density functionals NL3 [91], PK1 [92], TM1 [93], GM1 [94], and MTVTC [35] adopted here. Alternatively, the in-medium effects can be treated with density-dependent coupling constants according to the Typel-

Wolter ansatz [80], where

$$g_\xi(n_b) = g_\xi a_\xi \frac{1 + b_\xi(n_b/n_0 + d_\xi)^2}{1 + c_\xi(n_b/n_0 + d_\xi)^2}, \quad (3)$$

$$g_\rho(n_b) = g_\rho \exp[-a_\rho(n_b/n_0 + b_\rho)]. \quad (4)$$

Here $\xi = \sigma, \omega$ and the baryon number density $n_b = n_p + n_n$ with n_0 being the saturation density. In addition to the non-linear ones, we have also adopted the density-dependent covariant density functionals DD-LZ1 [95], DDME-X [96], PKDD [92], DD-ME2 [97], DD2 [98], and TW99 [80], where the nonlinear self-couplings in equation (2) vanish with $g_2 = g_3 = c_3 = 0$. For completeness, the parameter sets adopted in this work are listed in table 1, where $a_{\sigma,\omega} = 1$ and $b_{\sigma,\omega} = c_{\sigma,\omega} = a_\rho = 0$ if nonlinear self-couplings are adopted.

Carrying out standard variational procedure, the equations of motion for boson fields are fixed by

$$(-\nabla^2 + m_\sigma^2)\sigma = -g_\sigma n_s - g_2 \sigma^2 - g_3 \sigma^3, \quad (5)$$

$$(-\nabla^2 + m_\omega^2)\omega = g_\omega n_b + c_3 \omega^3, \quad (6)$$

$$(-\nabla^2 + m_\rho^2)\rho = \sum_{i=n,p} g_\rho \tau_i n_i, \quad (7)$$

$$-\nabla^2 A = e(n_p - n_e - n_\mu). \quad (8)$$

The scalar and vector densities are determined by

$$n_s = \sum_{i=n,p} \langle \bar{\psi}_i \psi_i \rangle = \sum_{i=n,p} \frac{M^{*3}}{2\pi^2} f\left(\frac{\nu_i}{M^*}\right), \quad (9)$$

$$n_i = \langle \bar{\psi}_i \gamma^0 \psi_i \rangle = \frac{\nu_i^3}{3\pi^2}, \quad (10)$$

where ν_i represents the Fermi momentum and $f(x) = x\sqrt{x^2 + 1} - \text{arcsch}(x)$. The total energy of the system is then fixed by

$$E = \int \langle \mathcal{T}_{00} \rangle d^3r, \quad (11)$$

with the energy momentum tensor

$$\begin{aligned} \langle \mathcal{T}_{00} \rangle = & \sum_{i=n,p,e,\mu} \frac{m_i^{*4}}{8\pi^2} [x_i(2x_i^2 + 1)\sqrt{x_i^2 + 1} - \text{arcsch}(x_i)] \\ & + \frac{1}{2}(\nabla\sigma)^2 + \frac{1}{2}m_\sigma^2\sigma^2 + \frac{1}{2}(\nabla\omega)^2 + \frac{1}{2}m_\omega^2\omega^2 + c_3\omega^4 \\ & + \frac{1}{2}(\nabla\rho)^2 + \frac{1}{2}m_\rho^2\rho^2 + \frac{1}{2}(\nabla A)^2 - U(\sigma, \omega), \end{aligned} \quad (12)$$

where $x_i \equiv \nu_i/m_i^*$ with $m_e^* = m_e = 0.511$ MeV and $m_\mu^* = m_\mu = 105.66$ MeV.

In the Thomas-Fermi approximation (TFA), the optimum density distributions $n_i(\vec{r})$ are fixed by minimizing the total energy E at given total particle numbers $N_i = \int n_i d^3r$, dimension D , and WS cell size R_W , which follows the constancy of chemical potentials, i.e.,

$$\begin{aligned} \mu_i(\vec{r}) = & \sqrt{\nu_i^2 + m_i^{*2}} + \Sigma^R + g_\omega \omega + g_\rho \tau_i \rho \\ & + q_i A = \text{constant}. \end{aligned} \quad (13)$$

Note that the ‘rearrangement’ term Σ^R needs to be considered if the density-dependent couplings are adopted in the

Lagrangian density [99], i.e.,

$$\Sigma^R = \frac{dg_\sigma}{dn_b} \sigma n_s + \frac{dg_\omega}{dn_b} \omega n_b + \frac{dg_\rho}{dn_b} \rho \sum_i \tau_i n_i. \quad (14)$$

2.2. Microscopic structures of neutron star matter

Neutron star matter at different densities exhibits various microscopic structures. At $n_b \lesssim 0.0003$ fm⁻³, neutron-rich nuclei and electrons form Coulomb lattices, which can be found in the outer crusts of neutron stars and white dwarfs. At larger densities, neutrons start to drip out and form neutron gas, then the neutron star matter is essentially a liquid-gas mixed phase and can be found in the inner crust region of a neutron star. As density increases, the liquid phase will eventually take non-spherical shapes that resemble pasta, which are hence referred to as nuclear pasta [28–32]. At densities $n_b \gtrsim 0.08$ fm⁻³, the core-crust transition takes place inside a neutron star, where the uniform phase is energetically more favorable for neutron star matter.

To obtain the microscopic structures of neutron star matter, we solve the Klein–Gordon equations and the density distributions iteratively inside a WS cell. Adopting the spherical and cylindrical approximations [35], the derivatives in the Klein–Gordon equations (5)–(8) are then reduced to one-dimensional, i.e.,

$$1D: \quad \nabla^2 \phi(\vec{r}) = \frac{d^2 \phi(r)}{dr^2}; \quad (15)$$

$$2D: \quad \nabla^2 \phi(\vec{r}) = \frac{d^2 \phi(r)}{dr^2} + \frac{1}{r} \frac{d\phi(r)}{dr}; \quad (16)$$

$$3D: \quad \nabla^2 \phi(\vec{r}) = \frac{d^2 \phi(r)}{dr^2} + \frac{2}{r} \frac{d\phi(r)}{dr}, \quad (17)$$

which can be solved via fast cosine transformation fulfilling the reflective boundary conditions at $r = 0$ and $r = R_W$ [100]. The density distributions of fermions are obtained with equation (13) fulfilling the β -stability condition $\mu_n = \mu_p + \mu_e = \mu_\mu$, where in practice we have adopted the imaginary time step method [101] to obtain the density profiles for the next iteration. Note that at each iteration, the total particle numbers fulfill the global charge neutrality condition

$$\int [n_p(\vec{r}) - n_e(\vec{r}) - n_\mu(\vec{r})] d^3r \equiv 0. \quad (18)$$

Different types of microscopic structures can be obtained with equations (15)–(17), i.e., droplet, rod, slab, tube, bubble, and uniform. At the given average baryon number density n_b , we then search for the energy minimum among six types of nuclear matter structures with optimum cell sizes R_W . Note that the effects of charge screening are included in our calculation with electrons moving freely within WS cells, which is expected to affect the microscopic structures of nuclear pasta [35]. With the density profiles fixed by fulfilling the convergence condition, the droplet size R_d and WS cell size R_W are then determined by

Table 1. The adopted parameters for the covariant density functionals with nonlinear self couplings (NL3 [91], PK1 [92], TM1 [93], GM1 [94], MTVTC [35]) and density-dependent couplings (DD-LZ1 [95], DDME-X [96], PKDD [92], DD-ME2 [97], DD2 [98], TW99 [80]).

	m_n MeV	m_p MeV	m_σ MeV	m_ω MeV	m_ρ MeV	g_σ	g_ω	g_ρ	g_2 fm^{-1}	g_3	c_3
NL3	939	939	508.1941	782.501	763	10.2169	12.8675	4.4744	-10.4307	-28.8851	0
PK1	938	938	511.198	783	770	10.0289	12.6139	4.6322	-7.2325	0.6183	71.3075
TM1	939.5731	938.2796	514.0891	784.254	763	10.3222	13.0131	4.5297	-8.1688	-9.9976	55.636
GM1	938	938	510	783	770	8.874 43	10.609 57	4.097 72	-9.7908	-6.63661	0
MTVTC	938	938	400	783	769	6.3935	8.7207	4.2696	-10.7572	-4.04529	0
DD-LZ1	938.9	938.9	538.619216	783	769	12.001 429	14.292 525	7.575 467	0	0	0
DDME-X	938.5	938.5	547.332728	783	763	10.706 722	13.338 846	3.619 020	0	0	0
PKDD	939.5731	938.2796	555.5112	783	763	10.7385	13.1476	4.2998	0	0	0
DD-ME2	938.5	938.5	550.1238	783	763	10.5396	13.0189	3.6836	0	0	0
DD2	939.56536	938.27203	546.212459	783	763	10.686 681	13.342 362	3.626 940	0	0	0
TW99	939	939	550	783	763	10.7285	13.2902	3.6610	0	0	0

	a_σ	b_σ	c_σ	d_σ	a_ω	b_ω	c_ω	d_ω	a_ρ	b_ρ
DD-LZ1	1.062748	1.763627	2.308928	0.379 957	1.059181	0.418273	0.538663	0.786649	0.776095	0
DDME-X	1.397043	1.334964	2.067122	0.401 565	1.393601	1.019082	1.605966	0.455586	0.620220	-1
PKDD	1.327423	0.435126	0.691666	0.694 210	1.342170	0.371167	0.611397	0.738376	0.183305	-1
DD-ME2	1.3881	1.0943	1.7057	0.4421	1.3892	0.9240	1.4620	0.4775	0.5647	-1
DD2	1.357630	0.634442	1.005358	0.575 810	1.369718	0.496475	0.817753	0.638452	0.983955	-1
TW99	1.365469	0.226061	0.409704	0.901 995	1.402488	0.172577	0.344293	0.983955	0.515000	-1

Table 2. Saturation properties of nuclear matter corresponding to the covariant density functionals indicated in table 1.

	n_0 fm ⁻³	B MeV	K MeV	J MeV	S MeV	L MeV	K_{sym} MeV
NL3	0.148	-16.25	271.7	204	37.4	118.6	101
PK1	0.148	-16.27	282.7	-27.8	37.6	115.9	55
TM1	0.145	-16.26	281.2	-285	36.9	110.8	34
GMI	0.153	-16.33	300.5	-216	32.5	94.0	18
MTVTC	0.153	-16.30	239.8	-513	32.5	89.6	-6.5
DD-LZ1	0.158	-16.06	230.7	1330	32.0	42.5	-20
DDME-X	0.152	-16.11	267.6	874	32.3	49.7	-72
PKDD	0.150	-16.27	262.2	-119	36.8	90.2	-81
DD-ME2	0.152	-16.13	250.8	477	32.3	51.2	-87
DD2	0.149	-16.02	242.7	169	31.7	55.0	-93
TW99	0.153	-16.24	240.2	-540	32.8	55.3	-125

$$R_d = \begin{cases} R_W \left(\frac{\langle n_p \rangle^2}{\langle n_p^2 \rangle} \right)^{1/D}, & \text{droplet-like} \\ R_W \left(1 - \frac{\langle n_p \rangle^2}{\langle n_p^2 \rangle} \right)^{1/D}, & \text{bubble-like} \end{cases}, \quad (19)$$

where $\langle n_p^2 \rangle = \int n_p^2(\vec{r}) d^3r / V$ and $\langle n_p \rangle = \int n_p(\vec{r}) d^3r / V$ with the WS cell volume

$$V = \begin{cases} \frac{4}{3} \pi R_W^3, & D = 3 \\ \pi a R_W^2, & D = 2 \\ a^2 R_W, & D = 1 \end{cases}. \quad (20)$$

In order for the volume to be finite for the slabs and rods/tubes at $D = 1$ and 2 , here we have adopted a finite cell size $a = 30$ fm. Meanwhile, as we decrease the density, it is found that R_W grows drastically and quickly exceeds the limit for any viable numerical simulations. In such cases, as was done in our previous study [69], at densities $n_b \lesssim 10^{-4} \text{ fm}^{-3}$ we divide the WS cell into a core with radius $R_{\text{in}} = 35.84$ fm and a spherical shell with constant densities.

3. Results and Discussion

3.1. Neutron star matter

The nuclear matter properties around the saturation density are illustrated in table 2 for various covariant density functionals adopted here, which cover a wide range for the incompressibility K , the skewness coefficient J , the symmetry energy S , the slope L and curvature parameter K_{sym} of the nuclear symmetry energy. Based on those functionals, we then investigate the EOSs and microscopic structures of neutron star matter adopting the numerical recipe introduced in section 2.

In figure 1 we present the obtained energy per baryon, pressure, and proton fraction for the most favorable nuclear shape with optimum WS cell size R_W . For comparison, the corresponding results for uniform matter are presented in the left panels as well. As we decrease the density, the proton fraction Y_p of the

uniform phase decreases and eventually vanishes for most of the functionals. Nevertheless, as indicated in table 1, adopting realistic neutron and proton masses for the covariant density functionals TM1, PKDD, and DD2, the proton fraction Y_p of the uniform phase does not vanish but increases to 1 as we decrease the density at $n_b \lesssim 10^{-4} \text{ fm}^{-3}$, which is reasonable as protons are more stable than neutrons. The contribution of electrons is then present in order to reach the local charge neutrality condition $n_p = n_e$. Once nonuniform nuclear structures emerge, the proton fraction Y_p deviates significantly from that of the uniform phase, which approaches to $Y_p = 0.43-0.45$ at vanishing densities. The energy per baryon is then reduced by up to 8 MeV. Note that the absolute values of the energy per baryon at vanishing densities are sensitive to the adopted nucleon masses, while the obtained binding energy for various functionals coincide with each other.

At vanishing densities, the pressure mainly comes from the contributions of electrons and is thus increasing with Y_p . Except for those adopting realistic nucleon masses, the obtained pressure for the nonuniform phase is larger than that of the uniform one as predicted by most of the functionals. The neutron drip densities n_d can be obtained by equating the chemical potential of neutrons with their mass, i.e., $\mu_n(n_d) = m_n$. The obtained values of n_d for various functionals are then indicated in table 3, where those with the density-dependent couplings generally predict smaller neutron drip densities compared with that of nonlinear ones. Then at $n_b \lesssim 10^{-4} \text{ fm}^{-3} < n_d$, neutron star matter is comprised of Coulomb lattices of nuclei and electrons, where similar values for the pressure are obtained with various functionals in this density range. In such cases, the EOSs of neutron star matter at $n_b \lesssim 10^{-4} \text{ fm}^{-3}$ generally coincide with each other except for the slight differences (within 0.1%) in the energy density due to the variations in the nucleon masses indicated in table 1.

At larger densities with $n_b \gtrsim n_d$, we note that the slope of the energy per baryon, pressure, and proton fraction change suddenly as neutron gas starts to coexist with the liquid phase of nuclear matter, which forms the nuclear pasta typically found in the inner crusts of neutron stars. In contrast to the stellar matter located in the outer crusts of neutron stars, as indicated in the left panel of figure 2, the EOSs of the pasta phase are sensitive to the adopted nuclear energy density functional. It is found that the EOSs obtained with nonlinear

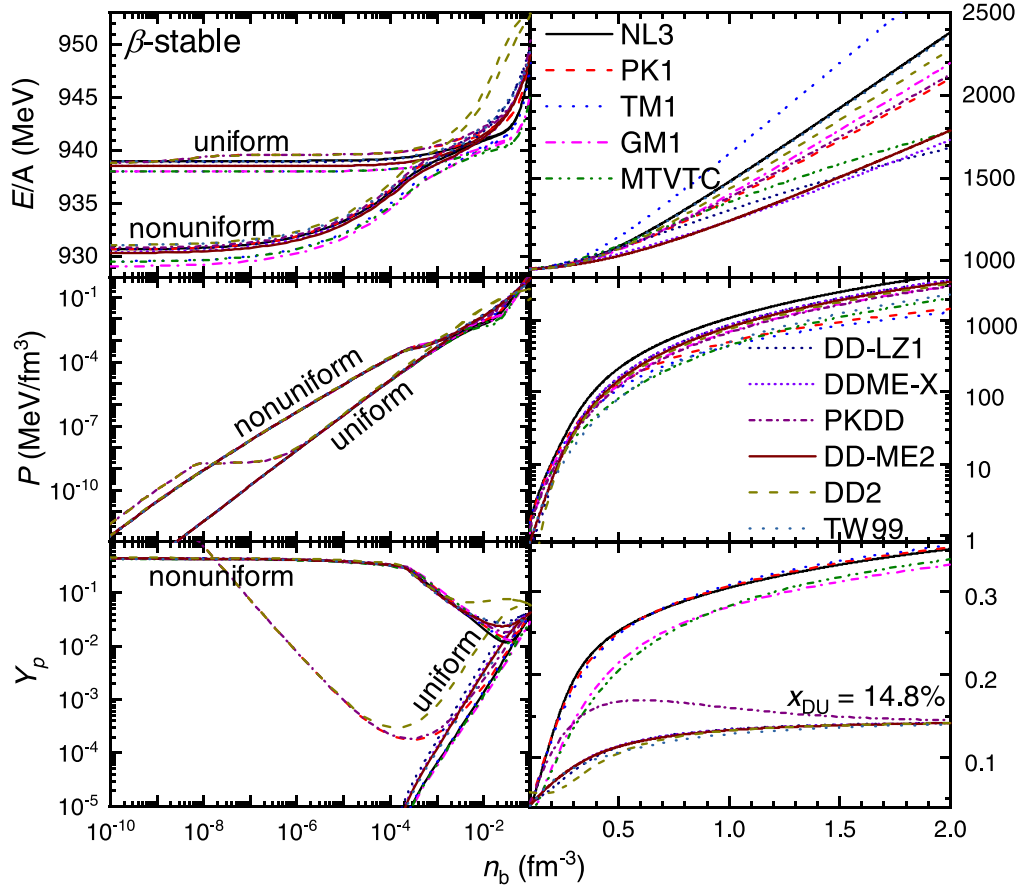


Figure 1. The energy per baryon E/A , pressure P , and proton fraction Y_p of neutron star matter as functions of baryon number density n_b , which are obtained with various covariant density functionals indicated in table 1. Both the uniform and nonuniform phases are illustrated in the left panels, while only uniform phases are presented in the right panels since the nonuniform one does not emerge. See the supplementary material for the corresponding EOS tables (available online at stacks.iop.org/CTP/74/095303/mmedia).

Table 3. Densities (in fm^{-3}) for shape transitions are obtained by varying the density in a step of 0.002 fm^{-3} . The neutron drip densities n_d obtained with $\mu_n(n_d) = m_n$ and critical densities n_{DU} for the occurrence of DU processes with $Y_p(n_{\text{DU}}) = 14.8\%$ are indicated as well.

Transition	NL3	PK1	TM1	GM1	MTVTC	DD-LZ1	DDME-X	PKDD	DD-ME2	DD2	TW99
n_d (10^{-4})	2.4	2.7	2.3	3.1	3.1	1.9	1.9	2.3	2.0	1.7	1.8
droplet-rod	—	—	—	—	—	0.059	0.065	—	0.063	0.041	0.063
rod-slab	—	—	—	—	—	0.065	0.073	—	0.071	0.057	0.071
slab-tube	—	—	—	—	—	0.069	—	—	0.073	0.087	0.075
tube-bubble	—	—	—	—	—	—	—	—	—	0.101	—
core-crust	0.057	0.061	0.061	0.067	0.061	0.071	0.077	0.065	0.075	0.111	0.077
n_{DU}	0.228	0.230	0.236	0.309	0.328	—	—	0.325	—	—	—

couplings become stiffer at the energy density $E/n_b \gtrsim 20 \text{ MeV fm}^{-3}$ ($n_b \gtrsim 0.02 \text{ fm}^{-3}$), while the EOSs obtained with density-dependent couplings vary more smoothly with density. In general, the relative uncertainty in the EOSs of the pasta phase grows with density and then decreases once it reaches the peak at $E/n_b \approx 20 \text{ MeV fm}^{-3}$. The corresponding differences in the EOSs at subsaturation densities are expected to affect the radii and crust thickness of neutron stars, which will be illustrated in figure 5. Note that for the functional DD2, the obtained results for nuclear pasta deviate significantly from other functionals. This is mainly because we have employed the single nucleus approximation (SNA)

and neglected the contributions of light clusters as initially proposed in [98]. For more suitable treatments adopting the extended nuclear statistical equilibrium model, one can refer to [102] with the publicly available EOS HS(DD2), which is more reasonable than the DD2 EOS presented in the left panel of figure 2 with a too large proton fraction.

If we further increase the density, the uniform phase becomes energetically more favorable once exceeding the core-crust transition densities indicated in table 3, e.g., $n_b \gtrsim 0.08 \text{ fm}^{-3}$. The corresponding energy per baryon, pressure, and proton fraction of neutron star matter are indicated in the right panels of figure 1. In contrast to the cases at

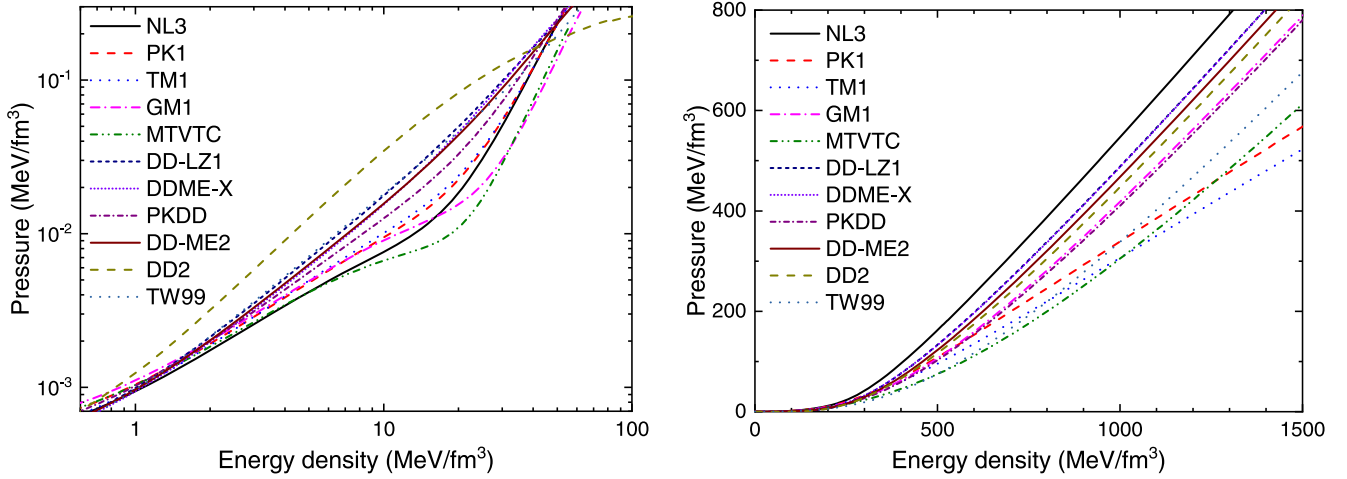


Figure 2. The EOSs for the pasta (left) and uniform (right) phases of neutron star matter, in correspondence to figure 1.

smaller densities, the uncertainties in those quantities grow drastically as density increases at $n_b \gtrsim 0.3 \text{ fm}^{-3}$, where the less constrained higher order coefficients such as L and K_{sym} start to play important roles. If the EOSs do not cross with each other, we note that the stiffness of EOS is directly linked to the maximum mass of neutron stars as indicated in figure 5. Despite their evident differences in the energy per baryon, as indicated in the right panel of figure 2, we note that the EOSs obtained with the functionals DD-LZ1 and DDME-X coincide with each other at $n_b \gtrsim 0.08 \text{ fm}^{-3}$.

The obtained proton fractions of neutron star matter at $n_b \gtrsim 0.08 \text{ fm}^{-3}$ show distinctive trends between the functionals with nonlinear self-couplings and density-dependent ones, which is attributed to the differences in the higher order coefficients L and K_{sym} of nuclear symmetry energy as indicated in table 2. It is found that Y_p increases with density if nonlinear self-couplings are adopted, while for density-dependent ones Y_p approaches a constant value (~ 0.14). It is worth mentioning that if isovector scalar channel (δ meson) are included in density-dependent covariant density functionals, the proton fraction may deviation from the trend and increase with density [88]. Meanwhile, we note that a peculiar density-dependent behavior of Y_p (reaching its maximum at $n_b \approx 0.5 \text{ fm}^{-3}$) is obtained with the functional PKDD, which is attributed to the large slope L but negative curvature parameter K_{sym} of nuclear symmetry energy. In principle, the proton fraction is directly connected to the most efficient cooling mechanism of neutron stars. Once the momentum conservation is fulfilled with $Y_p \gtrsim 14.8\%$, the direct Urca (DU) processes $n \rightarrow p + e^- + \bar{\nu}_e$ and $p + e^- \rightarrow n + \nu_e$ will take place and rapidly cools the neutron star down [103, 104]. As indicated in figure 1, the critical densities n_{DU} for the occurrence of DU processes can be obtained once $Y_p > 14.8\%$, where the corresponding values are presented in table 3. It is found that the DU processes only take place if the functionals with nonlinear self-couplings and PKDD are employed.

Besides the EOSs, the variation in the microscopic structures has significant implications on the transport and elastic properties of neutron star matter, which would in turn

affect various phenomena observed in neutron stars [105, 106]. In figure 3 we present the obtained microscopic structures of nonuniform neutron star matter corresponding to the EOSs in figures 1 and 2, where the proton number Z , WS cell radius R_W , and droplet size R_d are indicated. As density increases, the droplet, rod, slab, tube, bubble, and uniform phases appear sequentially for the nuclear pasta in neutron stars. The transition densities between different nuclear shapes are indicated in table 3. We note that for the functionals predicting large slope L of symmetry energy, only the droplet phase emerges for the nuclear pasta in β -equilibrium, while as indicated in figure 4 the core-crust transition densities n_t are smaller than those predicting smaller L as well. This is consistent with previous studies, where the proton number of nuclei, the core-crust transition density, and the onset density of non-spherical nuclei generally decrease with L [100, 107–111]. The obtained results with the functional NL3 and DD-ME2 generally coincide with those in [109] with slightly larger core-crust transition density, while those of TM1 coincide with [110]. Meanwhile, according to figure 4, it is evident that n_t also decreases with the curvature parameter K_{sym} of symmetry energy, which is closely related to the curvature-slope correlations [112, 113]. To show the consequences of adopting a functional that does not follow the curvature-slope correlation, in figure 4 we present the results predicted by FSUGarnet using the compressible liquid drop model [114], where the L - n_t correlation still holds approximately but not for the K_{sym} - n_t correlation. Note that the functional DD2 predicts a rather large n_t , which will be reduced if the extended nuclear statistical equilibrium model is adopted including the contributions of light clusters [102].

Similar to the EOSs of neutron star matter, as indicated in figure 3, the microscopic structures vary little with respect to the adopted functionals at $n_b \lesssim 10^{-4} \text{ fm}^{-3}$. For example, slightly different proton numbers and droplet sizes are obtained at vanishing densities (e.g., $n_b \approx 10^{-10} \text{ fm}^{-3}$) adopting various functionals, which vary within the ranges $Z \approx 28$ –35 and $R_d \approx 5$ –5.5 fm and increase with density at $n_b \lesssim 10^{-4} \text{ fm}^{-3}$. The obtained WS cell radius R_W is decreasing with density and is insensitive to the adopted functionals at $n_b \lesssim 10^{-4} \text{ fm}^{-3}$. We

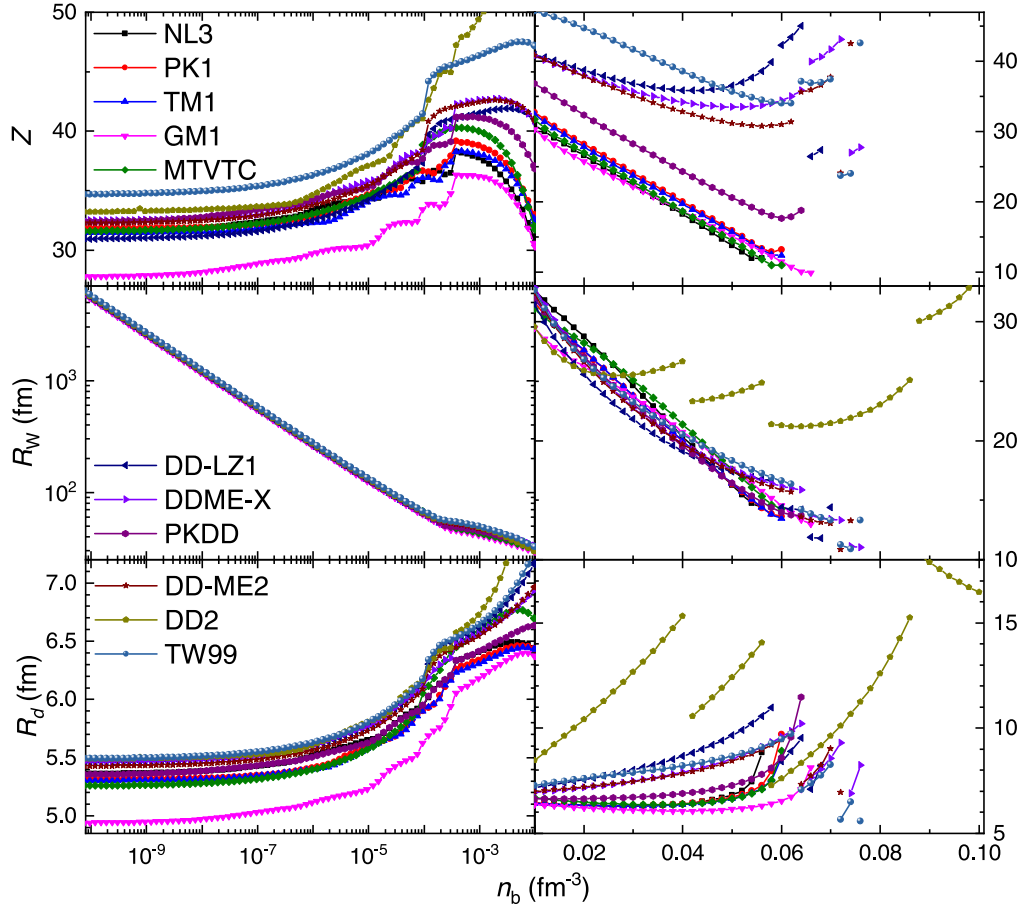


Figure 3. Proton number Z , WS cell radius R_W , and droplet size R_d for the nonuniform nuclear matter typically found in neutron star crusts, where the corresponding EOSs are indicated in figure 1.

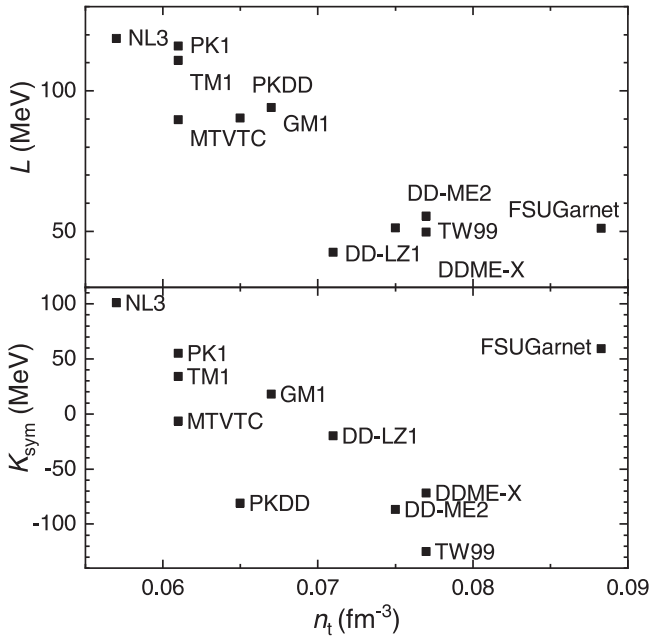


Figure 4. Crust-core transition densities n_t (indicated in table 3) obtained with various covariant density functionals and the corresponding slope L and curvature parameter K_{sym} of symmetry energy (indicated in table 2).

note that the differences in the microscopic structures start to grow once $n_b \gtrsim n_d$, where the values of Z and R_d as functions of density may exhibit different trends for various functionals. At larger densities with $n_b \gtrsim 0.01 \text{ fm}^{-3}$, the proton number Z and WS cell radius R_W are generally decreasing, while the droplet size R_d increases. Throughout the vast density range considered here, consistent with previous investigations [100, 107–111], the obtained values of Z and R_d approximately decrease with L if different functionals are adopted, while the values of R_W are close to each other. Note that rather large values of Z , R_d , and R_W are obtained with the functional DD2, which is mainly due to the SNA adopted here and neglecting light clusters.

3.2. Neutron stars

Based on the unified EOSs of neutron star matter presented in figures 1 and 2, the structures of neutron stars are obtained by solving the TOV equation

$$\frac{dP}{dr} = -\frac{GME(1+P/E)(1+4\pi r^3 P/M)}{r^2(1-2GM/r)}, \quad (21)$$

$$\frac{dM}{dr} = 4\pi E r^2, \quad (22)$$

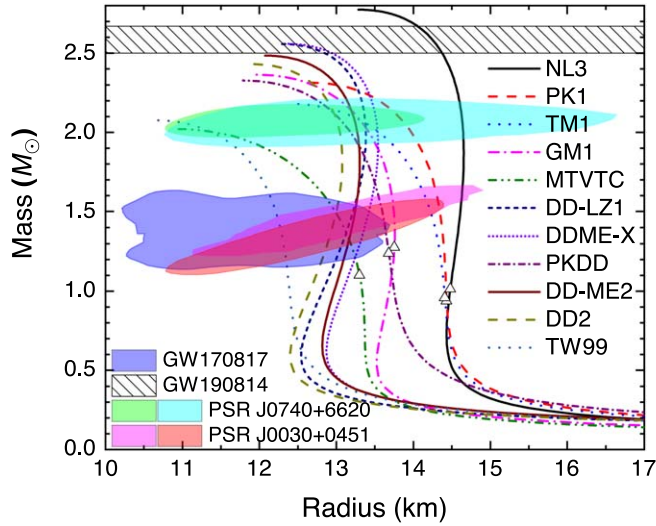


Figure 5. Mass-radius relations of neutron stars corresponding to the EOSs presented in figures 1 and 2, while the open triangles are the critical masses M_{DU} for DU processes. The shaded regions indicate the constraints from the binary neutron star merger event GW170817 within 90% credible region [63], the observational pulse-profiles in PSR J0030 + 0451 and PSR J0740 + 6620 within 68% credible region [64–67], and the mass ($2.50\text{--}2.67 M_{\odot}$) of a compact object observed in the gravitational-wave signal GW190814 in 90% credible region [115].

where $G = 6.707 \times 10^{-45} \text{ MeV}^{-2}$ is the gravity constant. In figure 5 we present the mass-radius relations of neutron stars corresponding to the covariant density functionals indicated in table 1. Various constraints from pulsar observations are indicated in figure 5, i.e., the binary neutron star merger event GW170817 [63], the simultaneous measurements of masses and radii for PSR J0030 + 0451 and PSR J0740 + 6620 [64–67], and the measured mass of a compact object involved in a compact binary coalescence from the gravitational-wave signal GW190814 [115]. The open triangles in figure 5 correspond to the critical masses M_{DU} for DU processes with the central densities exceeding n_{DU} . It is expected that the neutrino emissivity is enhanced significantly for neutron stars with $M > M_{\text{DU}}$ [116], which cool down too rapidly within just a few years [117]. It is found that the DU processes only take place if the functionals with nonlinear self-couplings and PKDD are employed ($M_{\text{DU}} \approx 0.9\text{--}1.3 M_{\odot}$), which have large slopes of symmetry energy with $L \gtrsim 90 \text{ MeV}$.

We note that all functionals predict neutron stars with maximum masses exceeding $2 M_{\odot}$ [62], while the functionals NL3, DD-LZ1, and DDME-X predict even larger maximum masses supporting the possibility that the secondary object observed in GW190814 is a neutron star [115]. Nevertheless, as indicated in table 2, the incompressibility, symmetry energy and its slope for nuclear matter obtained with the functional NL3 exceed the constraints from start-of-art studies [20, 24, 25], leading to neutron stars with too large radii and masses. A combined constraint on the masses and radii of neutron stars suggests that DD2, DD-LZ1, DD-ME2, and DDME-X are the most probable functionals that are consistent with observations. However, to support massive neutron stars, their skewness coefficients J are much larger than

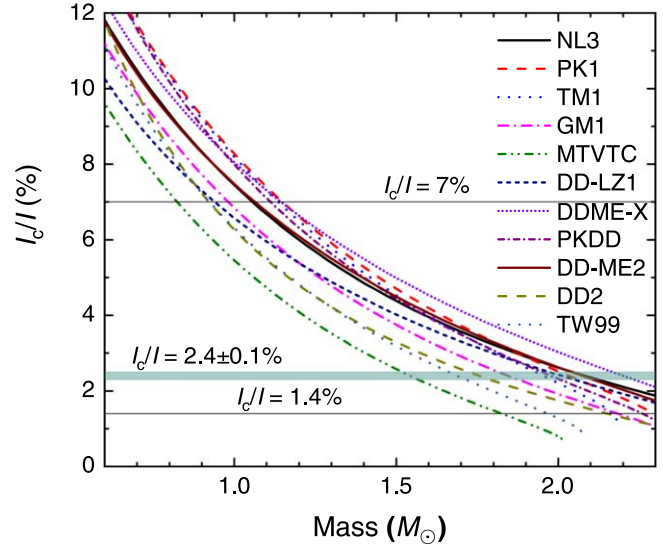


Figure 6. Crustal fraction of moment of inertia as a function of mass for neutron stars indicated in figure 5. The horizontal lines and band represent a possible constraint derived from the glitch activities in the Vela pulsar [12, 128–132].

expected, which was constrained to be $J = -700 \pm 500 \text{ MeV}$ from fits of generalized Skyrme force to breathing-mode energies [118] and $J = -390_{-70}^{+60} \text{ MeV}$ from empirical pressures in relativistic heavy-ion collisions [119]. The maximum masses of neutron stars obtained by the two functionals MTVTC and TW99 are close to $2 M_{\odot}$, while the corresponding radii are slightly small and located in the lower ends of the PSR J0740 + 6620 constraints [65, 67]. The functionals PKDD, GM1, TM1, PK1, and NL3 predict slightly too large radii according to the constraint derived from the binary neutron star merger event GW170817 [63], which are attributed to the much larger values for K and/or L as indicated in table 2. Nevertheless, if exotic phases with the emergence of new degrees of freedom such as mesons (π , K , etc.), heavy baryons (Δ , Λ , Σ , Ξ , Ω , etc.), and the deconfinement phase transition into quarks (u , d , s) were to take place, the corresponding EOSs would become softer, which effectively reduces the radii of compact stars and complies with the observational constraints [3, 4, 120–126].

It was argued that the sudden spin-ups (glitches) of pulsars are due to the angular momentum transfers from the superfluid component of a neutron star’s interior to its solid crust [127], whose characteristic properties could provide additional constraints on neutron star structures. In particular, the fractional crustal moment of inertia I_c/I can be measured with

$$\frac{I_c}{I} \gtrsim \frac{2\tau_c}{T} \sum_i \left(\frac{\Delta\Omega_p}{\Omega_p} \right)_i, \quad (23)$$

where τ_c represents the characteristic age of the pulsar, T the total time span for glitch monitoring, and $\Delta\Omega_p/\Omega_p$ the fractional frequency jump of glitches. To explain the glitches observed in the Vela pulsar, the fractional crustal moment of inertia was constrained to be $I_c/I \gtrsim 1.4\%$ [128]. However, it

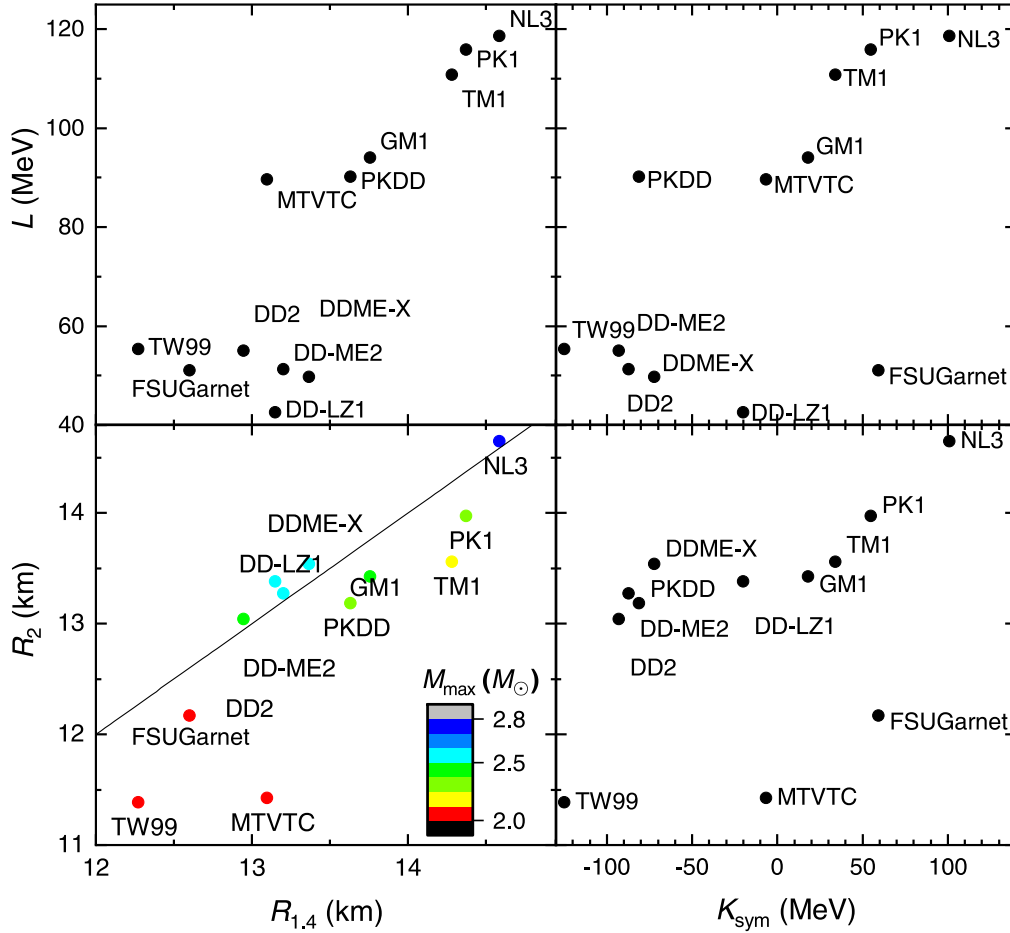


Figure 7. Correlations between neutron stars' radii ($R_{1.4}$ at $M = 1.4M_{\odot}$ and R_2 at $M = 2M_{\odot}$), the slope L and curvature parameter K_{sym} of nuclear symmetry energy obtained with various covariant density functionals.

was argued that the entrainment of superfluid neutrons by the solid crust could lower its mobility and increase the lower limit to $I_c/I \gtrsim 7\%$, causing the 'glitch crisis' where many nuclear EOSs fail to meet the constraint [129–131]. Nevertheless, it is worth mentioning that the entrainment effect may be suppressed if the pairing gap is of order or greater than the strength of the lattice potential [12], where the constraint can be reduced to $I_c/I \gtrsim 2.4 \pm 0.1\%$ [132].

For slowly rotating neutron stars, the fraction of crustal moment of inertia can be estimated with [128]

$$\frac{I_c}{I} \approx \frac{28\pi P_t R^3}{3M} \frac{1 - 1.67\beta - 0.6\beta^2}{\beta + \frac{2P_t}{n_t m_n} \left(\frac{1}{\beta} + 5 - 14\beta \right)}, \quad (24)$$

where P_t is the pressure at core-crust transition density n_t and $\beta = GM/R$ the compactness of a neutron star. The obtained results are then presented in figure 6, where the crustal moment of inertia is decreasing with mass. It is evident that I_c/I is sensitive to the EOS, and in particular, the crust one since it determines the mass and thickness of a neutron star's crust. Therefore a unified treatment for the EOSs of uniform (core) and nonuniform (crust) neutron star matter is essential to obtain accurately the radii, crust properties, core-crust transition density, as well as the corresponding microscopic structures. In order to meet the constraints of the Vela pulsar

as indicated by the horizontal lines and band, we note that a neutron star should not be more massive than a critical value, which varies with the EOSs and the effectiveness of the entrainment effect. Nevertheless, to distinguish the EOSs from one another, more detailed investigations on pulsar glitches are required in future studies.

To examine the possible correlations between the macroscopic neutron star structures and microscopic nuclear matter properties, in figure 7 we present the radii of neutron stars at $M = 1.4M_{\odot}$ and $2M_{\odot}$ as well as the slope L and curvature parameter K_{sym} of nuclear symmetry energy. It is evident that there are linear L - K_{sym} correlations in RMF models [112, 113], where K_{sym} increases with L . For the macroscopic neutron star structures, it is found that R_2 generally coincides with $R_{1.4}$ except for the two cases obtained with the functionals TW99 and MTVTC, where the maximum masses are close to $2M_{\odot}$ with $R_2 < R_{1.4}$. In such cases, if the radii $R_{1.4}$ are indeed close to R_2 as observed in NICER and XMM-Newton missions [64–67], then the maximum mass M_{max} of neutron stars could easily surpass $2.3M_{\odot}$ as indicated in the lower-left panel of figure 7, which approaches to the upper limit ($\leq 2.35M_{\odot}$) according to the numerical simulations of binary neutron star merger event GW170817 [133–135]. Meanwhile, we note that the maximum mass M_{max} generally increases with radius, which reaches $2.77M_{\odot}$ at $R_{1.4} = R_2 = 14.6$ km for the

functional NL3. The linear correlations between neutron stars' radii and L (K_{sym}) are also observed. In the top-left panel of figure 7 we find $R_{1.4}$ increases with L , which is consistent with previous investigations that the radius and tidal deformability are closely related to L [24, 113, 136–139]. At the same time, as indicated in the lower-right panel of figure 7, the radii of two-solar-mass neutron stars R_2 seem to have a better correlation with the higher order coefficient K_{sym} instead of L , which is attributed to the larger density range covered in those stars. Such kinds of correlations provide opportunities to constrain higher order coefficients of nuclear symmetry energy in the absence of strangeness via future radius measurements with both pulse-profile modeling [65, 67] and gravitational wave observations [63]. Nevertheless, it is worth mentioning that the correlations are mainly due to the particular choices of covariant density functionals. If we consider a functional that does not follow the L - K_{sym} correlation, such as FSUGarnet [114] indicated in figure 7, the K_{sym} - $R_{1.4,2}$ correlations become less evident than the L - $R_{1.4,2}$ correlations.

4. Conclusion

Based on the numerical recipe presented in our previous study [69], in this work we investigate systematically the EOSs and microscopic structures of neutron star matter in a vast density range with $n_b \approx 10^{-10} - 2 \text{ fm}^{-3}$ adopting various covariant density functionals (NL3 [91], PK1 [92], TM1 [93], GM1 [94], and MTVTC [35], DD-LZ1 [95], DDME-X [96], PKDD [92], DD-ME2 [97], DD2 [98], and TW99 [80]). All the results are obtained in a unified manner adopting Thomas-Fermi approximation, where spherical and cylindrical symmetries are assumed for the WS cells. The optimum configurations of neutron star matter in β -equilibrium are obtained by searching for the energy minimum among six types of nuclear matter structures (droplet, rod, slab, tube, bubble, and uniform) at fixed baryon number density n_b . The effects of charge screening are accounted for with electrons moving freely around the nucleus [35], where the proton number of nucleus Z , droplet size R_d , and WS cell size R_W become larger compared with the previous investigations neglecting the charge screening effects [69]. Note that we have adopted the SNA without any light clusters, which is not applicable for the functional DD2 as initially intended [98]. In such cases, we recommend [102] for a more suitable EOS HS(DD2) obtained with the extended nuclear statistical equilibrium model.

The neutron drip densities of neutron star matter are found to be $n_d \approx 2 \times 10^{-4} - 3 \times 10^{-4} \text{ fm}^{-3}$, where those with the density-dependent couplings generally predict smaller n_d than that of non-linear ones. At smaller densities, neutron star matter is comprised of Coulomb lattices of nuclei and electrons with pressure mainly coming from electrons, where the EOSs of neutron star matter generally coincide with each other (discrepancy within 0.1%). At $n_b > n_d$, the EOSs are sensitive to the adopted functionals, where the relative difference grows and reaches the peak at $n_b \approx 0.02 \text{ fm}^{-3}$. The relative uncertainty of the EOSs decreases and remains small

at $n_b \lesssim 0.3 \text{ fm}^{-3}$, which however grows drastically at larger densities.

For the microscopic structures, it is found that only the droplet (crust) and uniform (core) phases emerge if the covariant density functionals with nonlinear self-couplings are adopted, while non-spherical shapes (rod, slab, tube, and bubble) may appear if density-dependent couplings are employed with generally smaller slope L of symmetry energy. The corresponding core-crust transition densities n_t decrease with L as well. Meanwhile, the obtained droplet size R_d and proton number of nucleus Z approximately decrease with L , while the values of WS cell size R_W are close to each other. These observed trends generally coincide with previous investigations [100, 107–111]. Additionally, similar correlations with the curvature parameter K_{sym} are observed as well, which is closely related to the curvature-slope correlations [112, 113].

The neutron star structures are then investigated by adopting the unified EOSs. For all functionals considered in this work, the corresponding maximum masses of neutron stars exceed the two-solar-mass limit, while the functionals NL3, DD-LZ1, and DDME-X can even accommodate the mass of the secondary object observed in GW190814 [115]. A combined constraint on both the masses and radii from pulsar observations [63–67] suggests that DD2, DD-LZ1, DD-ME2, and DDME-X are the most probable functionals for describing neutron star matter, while those of MTVTC and TW99 predict radii close to the lower ends of the PSR J0740 + 6620 constraints [65, 67]. Nevertheless, in order to support massive neutron stars, the skewness coefficients J for DD2, DD-LZ1, DD-ME2, and DDME-X are much larger than expected [118, 119], which could be disentangled if the radius of PSR J0740 + 6620 [65, 67] and the maximum mass of neutron stars [133–135] can be measured with higher accuracy. The functionals PKDD, GM1, TM1, PK1, and NL3 predict slightly too large radii according to the GW170817 constraint [63], which can be reduced if exotic phases emerge at the center of neutron stars. Finally, we note there are approximate linear correlations between neutron stars' radii ($R_{1.4}$ at $M = 1.4M_\odot$ and R_2 at $M = 2M_\odot$) and the slope L of nuclear symmetry energy. Since we have adopted covariant density functionals with approximate curvature-slope correlations, the correlations of those quantities with the curvature parameter K_{sym} of symmetry energy are observed as well.

It was shown that the neutron star structures are sensitive to the EOSs both in the core and crust regions, where a unified description for neutron star matter is required [53, 56]. At the same time, the microscopic structures of neutron star matter play important roles in the corresponding transport and elastic properties, which affect various physical processes in neutron stars [105, 106]. Particularly, we have estimated the critical densities n_{DU} and neutron star masses M_{DU} at $Y_p = 14.8\%$, above which the DU processes will take place and cool the neutron star too rapidly within just a few years [103, 104]. We note that the DU processes only take place if functionals with $L \gtrsim 90 \text{ MeV}$ are adopted. The critical density lies in the range $n_{\text{DU}} \approx 0.23 - 0.33 \text{ fm}^{-3} > n_t$, so that the DU processes are sensitive to the core EOSs. Meanwhile, the crust

EOSs are closely connected to the fractional crustal moment of inertia I_c/I , which can be constrained by the characteristic properties of glitches observed in pulsars. It is shown that I_c/I is sensitive to the adopted EOS and in particular, the crust one, which provides opportunities to constrain neutron star structures and the corresponding EOS based on glitch monitoring. Further constraints may be obtained if we apply the current results to the investigations of other topics in pulsars such as asteroseismology [140–150], gravitational waves with respect to the strength of astromaterials [151–156], neutrino-pasta scattering [157], and the evolution of magnetic field [90, 158]. In such cases, the EOSs and microscopic structures of neutron star matter obtained in this work should be applicable for the investigations on the structures and evolutions of compact stars in a unified manner.

Acknowledgments

We would like to thank Prof. Nobutoshi Yasutake and Prof. Toshitaka Tatsumi for fruitful discussions. This work was supported by National SKA Program of China No. 2020SKA0120300, National Natural Science Foundation of China (Grant No. 11875052, No. 11873040, No. 11705163, and No. 11525524), the science research grants from the China Manned Space Project (No. CMS-CSST-2021-B11), the Youth Innovation Fund of Xiamen (No. 3502Z20206061), the Fundamental Research Funds for the Central Universities (Grant No. lzujbky-2021-sp36), and the National Key R&D Program of China No. 2018YFA0404402.

ORCID iDs

Cheng-Jun Xia  <https://orcid.org/0000-0002-3388-1137>

Bao Yuan Sun  <https://orcid.org/0000-0001-8958-9787>

References

- [1] Dutra M, Lourenço O, Sá Martins J S, Delfino A, Stone J R and Stevenson P D 2012 Skyrme interaction and nuclear matter constraints *Phys. Rev. C* **85** 035201
- [2] Dutra M, Lourenço O, Avancini S S, Carlson B V, Delfino A, Menezes D P, Providência C, Typel S and Stone J R 2014 Relativistic mean-field hadronic models under nuclear matter constraints *Phys. Rev. C* **90** 055203
- [3] Xia C-J, Maruyama T, Yasutake N, Tatsumi T, Shen H and Togashi H 2020 Systematic study on the quark-hadron mixed phase in compact stars *Phys. Rev. D* **102** 023031
- [4] Li A, Zhu Z-Y, Zhou E-P, Dong J-M, Hu J-N and Xia C-J 2020 Neutron star equation of state: Exemplary modeling and applications *JHEAP* **28** 19
- [5] Hebeler K 2021 Three-nucleon forces: Implementation and applications to atomic nuclei and dense matter *Phys. Rep.* **890** 1
- [6] Pons J A, Reddy S, Prakash M, Lattimer J M and Miralles J A 1999 Evolution of proto-neutron stars *Astrophys. J.* **513** 780
- [7] Horowitz C J, Pérez-García M A and Piekarewicz J 2004 Neutrino-‘pasta’ scattering: The opacity of nonuniform neutron-rich matter *Phys. Rev. C* **69** 045804
- [8] Lattimer J M 2012 The nuclear equation of state and neutron star masses *Annu. Rev. Nucl. Part. Sci.* **62** 485
- [9] Janka H-T 2012 Explosion mechanisms of core-collapse supernovae *Annu. Rev. Nucl. Part. Sci.* **62** 407
- [10] Bauswein A, Janka H-T, Hebeler K and Schwenk A 2012 Equation-of-state dependence of the gravitational-wave signal from the ring-down phase of neutron-star mergers *Phys. Rev. D* **86** 063001
- [11] Rueda J A, Ruffini R, Wu Y-B and Xue S-S 2014 Surface tension of the core-crust interface of neutron stars with global charge neutrality *Phys. Rev. C* **89** 035804
- [12] Watanabe G and Pethick C J 2017 Superfluid density of neutrons in the inner crust of neutron stars: new life for pulsar glitch models *Phys. Rev. Lett.* **119** 062701
- [13] Sotani H, Iida K and Oyamatsu K 2019 Astrophysical implications of double-layer torsional oscillations in a neutron star crust as a lasagna sandwich *Mon. Not. R. Astron. Soc.* **489** 3022
- [14] Köppel S, Bovard L and Rezzolla L 2019 A general-relativistic determination of the threshold mass to prompt collapse in binary neutron star mergers *Astrophys. J.* **872** L16
- [15] Baiotti L 2019 Gravitational waves from neutron star mergers and their relation to the nuclear equation of state *Prog. Part. Nucl. Phys.* **109** 103714
- [16] Schuetrumpf B, Martínez-Pinedo G and Reinhard P-G 2020 Survey of nuclear pasta in the intermediate-density regime: Structure functions for neutrino scattering *Phys. Rev. C* **101** 055804
- [17] Bauswein A, Blacker S, Vijayan V, Stergioulas N, Chatziioannou K, Clark J A, Bastian N-U F, Blaschke D B, Cierniak M and Fischer T 2020 Equation of state constraints from the threshold binary mass for prompt collapse of neutron star mergers *Phys. Rev. Lett.* **125** 141103
- [18] Gittins F, Andersson N and Pereira J P 2020 Tidal deformations of neutron stars with elastic crusts *Phys. Rev. D* **101** 103025
- [19] Préau E, Pascal A, Novak J and Oertel M 2021 What can be learned from a proto-neutron star’s mass and radius? *Mon. Not. R. Astron. Soc.* **505** 939
- [20] Shlomo S, Kolomietz V M and Colò G 2006 Deducing the nuclear-matter incompressibility coefficient from data on isoscalar compression modes *Eur. Phys. J. A* **30** 23
- [21] Li B-A and Han X 2013 Constraining the neutron-proton effective mass splitting using empirical constraints on the density dependence of nuclear symmetry energy around normal density *Phys. Lett. B* **727** 276
- [22] Oertel M, Hempel M, Klähn T and Typel S 2017 Equations of state for supernovae and compact stars *Rev. Mod. Phys.* **89** 015007
- [23] (PREX Collaboration) 2021 An accurate determination of the neutron skin thickness of ^{208}Pb through parity-violation in electron scattering *Phys. Rev. Lett.* **126** 172502
- [24] Zhang Y, Liu M, Xia C-J, Li Z and Biswal S K 2020 Constraints on the symmetry energy and its associated parameters from nuclei to neutron stars *Phys. Rev. C* **101** 034303
- [25] Essick R, Tews I, Landry P and Schwenk A 2021 Astrophysical constraints on the symmetry energy and the neutron skin of ^{208}Pb with minimal modeling assumptions *Phys. Rev. Lett.* **127** 192701
- [26] Yang S, Zhang B N and Sun B Y 2019 Critical parameters of the liquid-gas phase transition in thermal symmetric and asymmetric nuclear matter *Phys. Rev. C* **100** 054314
- [27] Yang S, Sun X D, Geng J, Sun B Y and Long W H 2021 Liquid-gas phase transition of thermal nuclear matter and the

- in-medium balance between nuclear attraction and repulsion *Phys. Rev. C* **103** 014304
- [28] Baym G, Pethick C and Sutherland P 1971 The ground state of matter at high densities: equation of state and stellar models *Astrophys. J.* **170** 299
- [29] Negele J W and Vautherin D 1973 Neutron star matter at sub-nuclear densities *Nucl. Phys. A* **207** 298
- [30] Ravenhall D G, Pethick C J and Wilson J R 1983 Structure of matter below nuclear saturation density *Phys. Rev. Lett.* **50** 2066
- [31] Hashimoto M-A, Seki H and Yamada M 1984 Shape of nuclei in the crust of neutron star *Prog. Theor. Phys.* **71** 320
- [32] Williams R and Koonin S 1985 Sub-saturation phases of nuclear matter *Nucl. Phys. A* **435** 844
- [33] Pethick C and Potekhin A 1998 Liquid crystals in the mantles of neutron stars *Phys. Lett. B* **427** 7
- [34] Oyamatsu K 1993 Nuclear shapes in the inner crust of a neutron star *Nucl. Phys. A* **561** 431
- [35] Maruyama T, Tatsumi T, Voskresensky D N, Tanigawa T and Chiba S 2005 Nuclear “pasta” structures and the charge screening effect *Phys. Rev. C* **72** 015802
- [36] Togashi H, Nakazato K, Takehara Y, Yamamuro S, Suzuki H and Takano M 2017 Nuclear equation of state for core-collapse supernova simulations with realistic nuclear forces *Nucl. Phys. A* **961** 78
- [37] Shen H, Toki H, Oyamatsu K and Sumiyoshi K 2011 Relativistic equation of state for core-collapse supernova simulations *Astrophys. J.* **197** 20
- [38] Magierski P and Heenen P-H 2002 Structure of the inner crust of neutron stars: Crystal lattice or disordered phase? *Phys. Rev. C* **65** 045804
- [39] Watanabe G, Sato K, Yasuoka K and Ebisuzaki T 2003 Structure of cold nuclear matter at subnuclear densities by quantum molecular dynamics *Phys. Rev. C* **68** 035806
- [40] Newton W G and Stone J R 2009 Modeling nuclear “pasta” and the transition to uniform nuclear matter with the 3D Skyrme-Hartree-Fock method at finite temperature: Core-collapse supernovae *Phys. Rev. C* **79** 055801
- [41] Nakazato K, Oyamatsu K and Yamada S 2009 Gyroid phase in nuclear pasta *Phys. Rev. Lett.* **103** 132501
- [42] Okamoto M, Maruyama T, Yabana K and Tatsumi T 2012 Three-dimensional structure of low-density nuclear matter *Phys. Lett. B* **713** 284
- [43] Schuetrumpf B, Klatt M A, Iida K, Maruhn J A, Mecke K and Reinhard P-G 2013 Time-dependent Hartree-Fock approach to nuclear “pasta” at finite temperature *Phys. Rev. C* **87** 055805
- [44] Schneider A S, Berry D K, Briggs C M, Caplan M E and Horowitz C J 2014 Nuclear “waffles” *Phys. Rev. C* **90** 055805
- [45] Schuetrumpf B, Klatt M A, Iida K, Schröder-Turk G E, Maruhn J A, Mecke K and Reinhard P-G 2015 Appearance of the single gyroid network phase in “nuclear pasta” matter *Phys. Rev. C* **91** 025801
- [46] Fattoyev F J, Horowitz C J and Schuetrumpf B 2017 Quantum nuclear pasta and nuclear symmetry energy *Phys. Rev. C* **95** 055804
- [47] Schuetrumpf B, Martínez-Pinedo G, Afibuzzaman M and Aktulga H M 2019 Survey of nuclear pasta in the intermediate-density regime: Shapes and energies *Phys. Rev. C* **100** 045806
- [48] Sagert I, Fann G I, Fattoyev F J, Postnikov S and Horowitz C J 2016 Quantum simulations of nuclei and nuclear pasta with the multiresolution adaptive numerical environment for scientific simulations *Phys. Rev. C* **93** 055801
- [49] Berry D K, Caplan M E, Horowitz C J, Huber G and Schneider A S 2016 Parking-garage structures in nuclear astrophysics and cellular biophysics *Phys. Rev. C* **94** 055801
- [50] Kashiwaba Y and Nakatsukasa T 2020 Coordinate-space solver for finite-temperature Hartree-Fock-Bogoliubov calculations using the shifted Krylov method *Phys. Rev. C* **101** 045804
- [51] Douchin F and Haensel P 2001 A unified equation of state of dense matter and neutron star structure *Astron. Astrophys.* **380** 151
- [52] Sharma B K, Centelles M, Viñas X, Baldo M and Burgio G F 2015 Unified equation of state for neutron stars on a microscopic basis *Astron. Astrophys.* **584** A103
- [53] Fortin M, Providência C, Raduta A R, Gulminelli F, Zdunik J L, Haensel P and Bejger M 2016 Neutron star radii and crusts: Uncertainties and unified equations of state *Phys. Rev. C* **94** 035804
- [54] Pearson J M, Chamel N, Potekhin A Y, Fantina A F, Ducoin C, Dutta A K and Goriely S 2018 Unified equations of state for cold non-accreting neutron stars with Brussels-Montreal functionals—I. Role of symmetry energy *Mon. Not. R. Astron. Soc.* **481** 2994
- [55] Viñas X, Gonzalez-Boquera C, Centelles M, Mondal C and Robledo L M 2021 Unified equation of state for neutron stars based on the gogny interaction *Symmetry* **13** 1613
- [56] Dinh Thi H, Carreau T, Fantina A F and Gulminelli F 2021 Uncertainties in the pasta-phase properties of catalysed neutron stars *Astron. Astrophys.* **654** A114
- [57] Newton W G, Balliet L, Budimir S, Crocombe G, Douglas B, Blake Head T, Rivera L, Langford Z and Sanford J 2022 Ensembles of unified crust and core equations of state in a nuclear-multimessenger astrophysics environment *Eur. Phys. J. A* **58** 69
- [58] Demorest P B, Pennucci T, Ransom S M, Roberts M S E and Hessels J W T 2010 A two-solar-mass neutron star measured using Shapiro delay *Nature* **467** 1081
- [59] Antoniadis J *et al* 2013 A massive pulsar in a compact relativistic binary *Science* **340** 1232323
- [60] Fonseca E *et al* 2016 The NANOGrav nine-year data set: mass and geometric measurements of binary millisecond pulsars *Astrophys. J.* **832** 167
- [61] Cromartie H T *et al* 2020 Relativistic Shapiro delay measurements of an extremely massive millisecond pulsar *Nat. Astron.* **4** 72
- [62] Fonseca E *et al* 2021 Refined mass and geometric measurements of the high-mass pSR J0740 + 6620 *Astrophys. J.* **915** L12
- [63] (LIGO Scientific and Virgo Collaborations) 2018 GW170817: Measurements of neutron star radii and equation of state *Phys. Rev. Lett.* **121** 161101
- [64] Riley T E *et al* 2019 A NICER View of PSR J0030 + 0451: millisecond pulsar parameter estimation *Astrophys. J.* **887** L21
- [65] Riley T E *et al* 2021 A NICER View of the massive pulsar PSR J0740 + 6620 informed by radio timing and XMM-newton spectroscopy *Astrophys. J.* **918** L27
- [66] Miller M C *et al* 2019 PSR J0030 + 0451 Mass and Radius from NICER Data and Implications for the Properties of Neutron Star Matter *Astrophys. J.* **887** L24
- [67] Miller M C *et al* 2021 The radius of PSR J0740 + 6620 from NICER and XMM-newton data *Astrophys. J.* **918** L28
- [68] Pang P T H, Tews I, Coughlin M W, Bulla M, Broeck C V D and Dietrich T 2021 Nuclear physics multimessenger astrophysics constraints on the neutron star equation of state: adding NICER’s PSR J0740 + 6620 measurement *Astrophys. J.* **922** 14
- [69] Xia C-J, Sun B Y, Maruyama T, Long W-H and Li A 2022 Unified nuclear matter equations of state constrained by the in-medium balance in density-dependent covariant density functionals *Phys. Rev. C* **105** 045803
- [70] Avancini S S, Menezes D P, Alloy M D, Marinelli J R, Moraes M M W and Providência C 2008 Warm and cold pasta phase in relativistic mean field theory *Phys. Rev. C* **78** 015802

- [71] Avancini S S, Brito L, Marinelli J R, Menezes D P, de Moraes M M W, Providência C and Santos A M 2009 Nuclear 'pasta' phase within density dependent hadronic models *Phys. Rev. C* **79** 035804
- [72] Gupta N and Arumugam P 2013 Pasta phases in neutron stars studied with extended relativistic mean field models *Phys. Rev. C* **87** 028801
- [73] Meng J (ed) 2016 *Relativistic Density Functional for Nuclear Structure, International Review of Nuclear Physics* 10 (Singapore: World Scientific Pub Co Pte Lt) (<https://doi.org/10.1142/9872>)
- [74] Reinhard P-G 1989 The relativistic mean-field description of nuclei and nuclear dynamics *Rep. Prog. Phys.* **52** 439
- [75] Ring P 1996 Relativistic mean field theory in finite nuclei *Prog. Part. Nucl. Phys.* **37** 193
- [76] Meng J, Toki H, Zhou S, Zhang S, Long W and Geng L 2006 Relativistic continuum Hartree Bogoliubov theory for ground-state properties of exotic nuclei *Prog. Part. Nucl. Phys.* **57** 470
- [77] Paar N, Vretenar D, Khan E and Colò G 2007 Exotic modes of excitation in atomic nuclei far from stability *Rep. Prog. Phys.* **70** R02
- [78] Meng J and Zhou S G 2015 Halos in medium-heavy and heavy nuclei with covariant density functional theory in continuum *J. Phys. G: Nucl. Part. Phys.* **42** 093101
- [79] Chen C, Sun Q-K, Li Y-X and Sun T-T 2021 Possible shape coexistence in Ne isotopes and the impurity effect of Λ hyperon *Sci. China Phys. Mech. Astron.* **64** 282011
- [80] Typel S and Wolter H 1999 Relativistic mean field calculations with density-dependent meson-nucleon coupling *Nucl. Phys. A* **656** 331
- [81] Vretenar D, Pöschl W, Lalazissis G A and Ring P 1998 Relativistic mean-field description of light Λ hypernuclei with large neutron excess *Phys. Rev. C* **57** R1060
- [82] Lu B-N, Zhao E-G and Zhou S-G 2011 Quadrupole deformation (β , γ) of light Λ hypernuclei in a constrained relativistic mean field model: Shape evolution and shape polarization effect of the Λ hyperon *Phys. Rev. C* **84** 014328
- [83] Glendenning N 2000 *Compact Stars. Nuclear Physics, Particle Physics, and General Relativity* II edn (Berlin: Springer) www.springer.com/cn/book/9780387989778
- [84] Ban S F, Li J, Zhang S Q, Jia H Y, Sang J P and Meng J 2004 Density dependencies of interaction strengths and their influences on nuclear matter and neutron stars in relativistic mean field theory *Phys. Rev. C* **69** 045805
- [85] Weber F, Negreiros R, Rosenfield P and Stejner M 2007 Pulsars as astrophysical laboratories for nuclear and particle physics *Prog. Part. Nucl. Phys.* **59** 94
- [86] Long W H, Sun B Y, Hagino K and Sagawa H 2012 Hyperon effects in covariant density functional theory and recent astrophysical observations *Phys. Rev. C* **85** 025806
- [87] Sun T T, Sun B Y and Meng J 2012 BCS-BEC crossover in nuclear matter with the relativistic Hartree-Bogoliubov theory *Phys. Rev. C* **86** 014305
- [88] Wang S, Zhang H F and Dong J M 2014 Neutron star properties in density-dependent relativistic mean field theory with consideration of an isovector scalar meson *Phys. Rev. C* **90** 055801
- [89] Fedoseev A and Lenske H 2015 Thermal properties of asymmetric nuclear matter *Phys. Rev. C* **91** 034307
- [90] Gao Z-F, Wang N, Shan H, Li X-D and Wang W 2017 The dipole magnetic field and spin-down evolutions of the high braking index pulsar PSR J1640-4631 *Astrophys. J.* **849** 19
- [91] Lalazissis G A, König J and Ring P 1997 New parametrization for the Lagrangian density of relativistic mean field theory *Phys. Rev. C* **55** 540
- [92] Long W-H, Meng J, Giai N V and Zhou S-G 2004 New effective interactions in relativistic mean field theory with nonlinear terms and density-dependent meson-nucleon coupling *Phys. Rev. C* **69** 034319
- [93] Sugahara Y and Toki H 1994 Relativistic mean-field theory for unstable nuclei with non-linear σ and ω terms *Nucl. Phys. A* **579** 557
- [94] Glendenning N K and Moszkowski S A 1991 Reconciliation of neutron-star masses and binding of the Λ in hypernuclei *Phys. Rev. Lett.* **67** 2414
- [95] Wei B, Zhao Q, Wang Z-H, Geng J, Sun B-Y, Niu Y-F and Long W-H 2020 Novel relativistic mean field Lagrangian guided by pseudo-spin symmetry restoration *Chin. Phys. C* **44** 074107
- [96] Taminah A, Agbemava S, Afanasjev A and Ring P 2020 Parametric correlations in energy density functionals *Phys. Lett. B* **800** 135065
- [97] Lalazissis G A, Nikšić T, Vretenar D and Ring P 2005 New relativistic mean-field interaction with density-dependent meson-nucleon couplings *Phys. Rev. C* **71** 024312
- [98] Typel S, Röpke G, Klähn T, Blaschke D and Wolter H H 2010 Composition and thermodynamics of nuclear matter with light clusters *Phys. Rev. C* **81** 015803
- [99] Lenske H and Fuchs C 1995 Rearrangement in the density dependent relativistic field theory of nuclei *Phys. Lett. B* **345** 355
- [100] Xia C-J, Maruyama T, Yasutake N, Tatsumi T and Zhang Y-X 2021 Nuclear pasta structures and symmetry energy *Phys. Rev. C* **103** 055812
- [101] Levit S 1984 The imaginary time step method for Thomas-Fermi equations *Phys. Lett. B* **139** 147
- [102] Fischer T, Hempel M, Sagert I, Suwa Y and Schaffner-Bielich J 2014 Symmetry energy impact in simulations of core-collapse supernovae *Eur. Phys. J. A* **50** 46
- [103] Klähn T *et al* 2006 Constraints on the high-density nuclear equation of state from the phenomenology of compact stars and heavy-ion collisions *Phys. Rev. C* **74** 035802
- [104] Page D, Geppert U and Weber F 2006 The cooling of compact stars *Nucl. Phys. A* **777** 497
- [105] Chamel N and Haensel P 2008 Physics of neutron star crusts *Living Rev. Rel.* **11** 10
- [106] Caplan M E and Horowitz C J 2017 Colloquium: Astromaterial science and nuclear pasta *Rev. Mod. Phys.* **89** 041002
- [107] Oyamatsu K and Iida K 2007 Symmetry energy at subnuclear densities and nuclei in neutron star crusts *Phys. Rev. C* **75** 015801
- [108] Xu J, Chen L-W, Li B-A and Ma H-R 2009 Nuclear constraints on properties of neutron star crusts *Astrophys. J.* **697** 1549
- [109] Grill F, Providência C and Avancini S S 2012 Neutron star inner crust and symmetry energy *Phys. Rev. C* **85** 055808
- [110] Bao S S and Shen H 2015 Impact of the symmetry energy on nuclear pasta phases and crust-core transition in neutron stars *Phys. Rev. C* **91** 015807
- [111] Shen H, Ji F, Hu J and Sumiyoshi K 2020 Effects of symmetry energy on the equation of state for simulations of core-collapse supernovae and neutron-star mergers *Astrophys. J.* **891** 148
- [112] Pais H and Stone J R 2012 Exploring the nuclear pasta phase in core-collapse supernova matter *Phys. Rev. Lett.* **109** 151101
- [113] Li B-A and Magno M 2020 Curvature-slope correlation of nuclear symmetry energy and its imprints on the crust-core transition, radius, and tidal deformability of canonical neutron stars *Phys. Rev. C* **102** 045807
- [114] Parmar V, Das H C, Kumar A, Sharma M K and Patra S K 2022 Crustal properties of a neutron star within an effective relativistic mean-field model *Phys. Rev. D* **105** 043017

- [115] Abbott R *et al* 2020a GW190814: gravitational waves from the coalescence of a 23 solar mass black hole with a 2.6 solar mass compact object *Astrophys. J.* **896** L44
- [116] Spinella W M, Weber F, Orsaria M G and Contrera G A 2018 Neutrino emissivity in the quark-hadron mixed phase *Universe* **4** 64
- [117] Blaschke D, Grigorian H and Voskresensky D N 2004 Cooling of neutron stars. Hadronic model *Astron. Astrophys.* **424** 979
- [118] Farine M, Pearson J and Tondeur F 1997 Nuclear-matter incompressibility from fits of generalized Skyrme force to breathing-mode energies *Nucl. Phys. A* **615** 135
- [119] Xie W-J and Li B-A 2021 Bayesian inference of the incompressibility, skewness and kurtosis of nuclear matter from empirical pressures in relativistic heavy-ion collisions *J. Phys. G: Nucl. Part. Phys.* **48** 025110
- [120] Baym G, Hatsuda T, Kojo T, Powell P D, Song Y and Takatsuka T 2018 From hadrons to quarks in neutron stars: a review *Rep. Prog. Phys.* **81** 056902
- [121] Sun T-T, Zhang S-S, Zhang Q-L and Xia C-J 2019 Strangeness and Δ resonance in compact stars with relativistic-mean-field models *Phys. Rev. D* **99** 023004
- [122] Dexheimer V, Gomes R O, Klähn T, Han S and Salinas M 2021a GW190814 as a massive rapidly rotating neutron star with exotic degrees of freedom *Phys. Rev. C* **103** 025808
- [123] Dexheimer V, Marquez K D and Menezes D P 2021b Delta baryons in neutron-star matter under strong magnetic fields *Eur. Phys. J. A* **57** 216
- [124] Sun T-T, Zheng Z-Y, Chen H, Burgio G F and Schulze H-J 2021 Equation of state and radial oscillations of neutron stars *Phys. Rev. D* **103** 103003
- [125] Tu Z-H and Zhou S-G 2022 Effects of the ϕ Meson on the Properties of Hyperon Stars in the Density-dependent Relativistic Mean Field Model *Astrophys. J.* **925** 16
- [126] Sun X-D, Miao Z-Q, Sun B-Y and Li A 2022 arXiv:2205.10631
- [127] Anderson P W and Itoh N 1975 Pulsar glitches and restlessness as a hard superfluidity phenomenon *Nature* **256** 25
- [128] Link B, Epstein R I and Lattimer J M 1999 Pulsar constraints on neutron star structure and equation of state *Phys. Rev. Lett.* **83** 3362
- [129] Andersson N, Glampedakis K, Ho W C G and Espinoza C M 2012 Pulsar glitches: the crust is not enough *Phys. Rev. Lett.* **109** 241103
- [130] Chamel N 2012 Neutron conduction in the inner crust of a neutron star in the framework of the band theory of solids *Phys. Rev. C* **85** 035801
- [131] Li A, Dong J M, Wang J B and Xu R X 2016 Structures of the vela pulsar and the glitch crisis from the brueckner theory *Astrophys. J. Suppl. Ser.* **223** 16
- [132] Li A and Wang R 2017 Pulsar glitch and nuclear EoS: Applicability of superfluid model *IAUS* **13** 360
- [133] Rezzolla L, Most E R and Weih L R 2018 Using Gravitational-wave Observations and Quasi-universal Relations to Constrain the Maximum Mass of Neutron Stars *Astrophys. J.* **852** L25
- [134] Ruiz M, Shapiro S L and Tsokaros A 2018 GW170817, general relativistic magnetohydrodynamic simulations, and the neutron star maximum mass *Phys. Rev. D* **97** 021501
- [135] Shibata M, Zhou E, Kiuchi K and Fujibayashi S 2019 Constraint on the maximum mass of neutron stars using GW170817 event *Phys. Rev. D* **100** 023015
- [136] Zhu Z-Y, Zhou E-P and Li A 2018 Neutron star equation of state from the quark level in light of GW170817 *Astrophys. J.* **862** 98
- [137] Tsang M, Lynch W, Danielewicz P and Tsang C 2019 Symmetry energy constraints from GW170817 and laboratory experiments *Phys. Lett. B* **795** 533
- [138] Dexheimer V, de Oliveira Gomes R, Schramm S and Pais H 2019 What do we learn about vector interactions from GW170817? *J. Phys. G: Nucl. Part. Phys.* **46** 034002
- [139] Zhang N-B and Li B-A 2019 Extracting nuclear symmetry energies at high densities from observations of neutron stars and gravitational waves *Eur. Phys. J. A* **55** 39
- [140] Kouveliotou C *et al* 1998 An X-ray pulsar with a superstrong magnetic field in the soft gamma-ray repeater SGR 1806-20 *Nature* **393** 235
- [141] Hurley K *et al* 1999 A Giant, periodic flare from the soft gamma repeater SGR1900 + 14 *Nature* **397** 41
- [142] Hansen C J and Cioffi D F 1980 Torsional oscillations in neutron star crusts *Astrophys. J.* **238** 740
- [143] Schumaker B L and Thorne K S 1983 Torsional oscillations of neutron stars *Mon. Not. R. Astron. Soc.* **203** 457
- [144] McDermott P N, van Horn H M and Hansen C J 1988 Nonradial Oscillations of Neutron Stars *Astrophys. J.* **325** 725
- [145] Strohmayer T, Ogata S, Iyemori H, Ichimaru S and van Horn H M 1991 The shear modulus of the neutron star crust and nonradial oscillations of neutron stars *Astrophys. J.* **375** 679
- [146] Passamonti A and Andersson N 2012 Towards real neutron star seismology: accounting for elasticity and superfluidity *Mon. Not. R. Astron. Soc.* **419** 638
- [147] Gabler M, Cerdá-Durán P, Stergioulas N, Font J A and Müller E 2018 Constraining properties of high-density matter in neutron stars with magneto-elastic oscillations *Mon. Not. R. Astron. Soc.* **476** 4199
- [148] Sotani H, Nakazato K, Iida K and Oyamatsu K 2012 Probing the equation of state of nuclear matter via neutron star asteroseismology *Phys. Rev. Lett.* **108** 201101
- [149] Sotani H, Iida K and Oyamatsu K 2016 Probing nuclear bubble structure via neutron star asteroseismology *Mon. Not. R. Astron. Soc.* **464** 3101
- [150] Kozhberov A A and Yakovlev D G 2020 Deformed crystals and torsional oscillations of neutron star crust *Mon. Not. R. Astron. Soc.* **498** 5149
- [151] Horowitz C J and Kadau K 2009 Breaking strain of neutron star crust and gravitational waves *Phys. Rev. Lett.* **102** 191102
- [152] Chugunov A I and Horowitz C J 2010 Breaking stress of neutron star crust *Mon. Not. R. Astron. Soc.* **407** L54
- [153] Horowitz C J 2010 Gravitational waves from low mass neutron stars *Phys. Rev. D* **81** 103001
- [154] Caplan M E, Schneider A S and Horowitz C J 2018 Elasticity of nuclear pasta *Phys. Rev. Lett.* **121** 132701
- [155] Baiko D A and Chugunov A I 2018 Breaking properties of neutron star crust *Mon. Not. R. Astron. Soc.* **480** 5511
- [156] Abbott R *et al* 2020b Gravitational-wave constraints on the equatorial ellipticity of millisecond pulsars *Astrophys. J.* **902** L21
- [157] Horowitz C J, Berry D K, Caplan M E, Fischer T, Lin Z, Newton W G, O'Connor E and Roberts L F 2016 Nuclear pasta and supernova neutrinos at late times arXiv:1611.10226 [astro-ph.HE]
- [158] Pons J A, Viganò D and Rea N 2013 A highly resistive layer within the crust of X-ray pulsars limits their spin periods *Nat. Phys.* **9** 431